The Effect of Surface Termination on Dielectric Non-linearity in Potassium Sodium Niobate Thin Films

Soňa Hříbalová[1,3,*], Betul Akkopru-Akgun[2,3,*], Susan Trolier-McKinstry[2,3]

[1]*Department of Glass and Ceramics, University of Chemistry and Technology, Prague, Prague 166 28, Czech Republic*
[2]*Center for Dielectrics and Piezoelectrics, Millennium Science Complex, Penn State University, University Park, PA 16802*
[3]*Department of Materials Science and Engineering, Penn State University, University Park, PA 16802*

*Authors Soňa Hříbalová and Betul Akkopru-Akgun contributed equally to this work.

Abstract

The impact of alkali-rich and alkali-depleted surface terminations on dielectric non-linearity and ferroelectric properties was investigated in sputtered $K_{0.5}Na_{0.5}NbO_3$ (KNN) films. For the alkali depleted surface termination, a ~3 nm thick amorphous interfacial layer was found near the top electrode. The presence of a non-ferroelectric interfacial layer reduces both the net remanent (P_r) and maximum polarization (P_{max}) while increasing the coercive field (E_c) in the KNN films. P_{max} decreased from 31.5 to 30.3 μC/cm², likely due to reduced electric field in the bulk of the film. The influence of the interfacial layer on dielectric properties was evaluated using a capacitor in series model. After removing the effects of the interfacial layer, the Rayleigh coefficients ε_{init} and α increased by 11 and 47%, respectively. The interfacial layer has more impact on irreversible domain wall motion than on reversible contributions to the relative permittivity. It is believed that this occurs because a higher concentration of defects, such as $V'_{K,Na}$ or $V_O^{\cdot\cdot}$, associated with the alkali-depleted interfacial layer generates internal fields that pin domain walls. Alkali depleted surface terminations also produce a higher pseudo-activation energy for polarization reversal compared to films with alkali rich terminations, associated with deeper potential wells in the material's energy landscape.

Keywords: Potassium sodium niobate thin films; surface termination; dielectric nonlinearity, Rayleigh, Preisach

1. Introduction

Ferroelectric thin films are widely used in applications including capacitors, sensors, actuators, and optical devices.[1] While many ferroelectric films, such as lead zirconate titanate (PZT),[2] contain lead, the use of lead-based materials and the environmental and health risks associated with lead exposure are of growing concern. Consequently, there is significant legislative pressure to replace lead-containing piezoelectrics with lead-free materials.[3] Potassium sodium niobate ($K_xNa_{1-x}NbO_3$, KNN) ferroelectric films have been extensively studied as a lead-free alternative to PZT due to its relatively high piezoelectric coefficients and a high Curie temperature relative to other lead-free ferroelectric films.[4-6]

In undoped $K_{0.5}Na_{0.5}NbO_3$ single crystals, the reported remanent polarization was 17 $\mu C/cm^2$,[7] the coercive field (E_c) was 24 kV/cm [7] and the relative permittivity was 1015 for [131]-oriented single crystal and 650 for [323]-oriented single crystal at 100 kHz.[7] Zhang et al. published an extensive review of the properties of KNN-based thin films.[3] The relative permittivity range reported for thin films is 185 and 685.[3,8,9]

It is notable that during processing of both KNN films and bulk ceramics, K_2O and Na_2O can volatilize, leading to the formation of secondary phases and alkali or oxygen vacancies.[2,3,10,11] Moreover, KNN can react with atmospheric CO_2 to form carbonates.[12] Water-induced degradation is also problematic due to the relatively high solubility of potassium and sodium ions in aqueous solutions.[13] Recent studies have demonstrated a significant negative effect of a small amount of hygroscopic compounds in KNN on its dielectric and piezoelectric properties, even when these compounds are not detectable by X-ray diffraction. It has been reported that the presence of hygroscopic compounds resulted in a tanδ of 146% compared to 6.3% and a d_{33} of 80 ± 20 pC/N compared to 149 ± 4 pC/N for samples without such compounds. Furthermore, upon aging in humidity, samples containing hygroscopic compounds completely degraded after two weeks in a humid chamber, whereas their counterparts maintained their shape and properties. If these challenges are not addressed, KNN exhibits poor electrical and electromechanical properties, low fatigue resistance and stability issues.[11,14,15]

The fabrication process and subsequent integration of KNN films into piezoMEMS, utilizing techniques such as dry etching, wet etching, and post-annealing, can further modify the surface termination. An alkali depleted non-stoichiometric layer can form at the KNN surface due to the volatilization of alkali oxides upon annealing, or the leaching of alkali ions during chemical exposure. This in turn impacts the observed dielectric and ferroelectric properties.[16] It has been reported that an interfacial non-ferroelectric layer between the electrode and the ferroelectric thin film inhibits charge compensation, creating a depolarization field.[17] Moreover, interfacial layers may cause imprint (i.e. a horizontal shift in the hysteresis loop), hindering data retention and reducing reliability in ferroelectric non-volatile memories).[18-21] The development of the imprint has been attributed to ionic defects such as oxygen vacancies that induce domain pinning, and to the formation of non-switching layers.[16,18,22-24] Additionally, any interfacial layer may act as a capacitor in series,

lowering the effective electric field experienced by the rest of the film, further altering the response of the material.

For potassium sodium niobate-based thin films, the manner in which surface termination affects film properties is largely unknown. However, given that changes in the alkali content would be expected at the surface due to volatilization, it is possible that surface layers play an important role in the properties.[11] For example, a recent study on the interactions between point, line and planar defects and secondary phases in KNN thin films demonstrated that point and extended defects formed by local non-stoichiometry strongly interact with the surrounding lattice, significantly affecting the polarization.[15] Furthermore, the effects of electrical degradation on intrinsic and extrinsic electrical properties have yet to be thoroughly examined. Presently, the literature offers limited insight, with a few studies addressing DC resistance degradation.[25] This study explored the impact of surface termination, with a particular emphasis on interfacial layer, on the dielectric and ferroelectric characteristics of KNN thin films. In this study, sputtered potassium sodium niobate ($K_{0.5}Na_{0.5}NbO_3$) thin films, with alkali-rich and alkali-depleted surface termination were supplied by SCIOCS Co. Ltd. The variations in dielectric and ferroelectric properties attributable to the interfacial layer in alkali-depleted KNN films were explored utilizing Rayleigh and Preisach analyses, as well as polarization-electric field (P-E) measurements across a temperature range of 10-300K.

2. Experimental Procedure

$K_{0.5}Na_{0.5}NbO_3$ (KNN) films with a thickness of 1.7 μm were provided by SCIOCS Co. Ltd. The KNN films were grown on Pt/ZnO/SiO_2/Si substrates using RF magnetron sputtering, as described elsewhere.[26] A ZnO layer was included to enhance adhesion between the Pt electrode and the SiO_2/Si substrate.[48] Post-deposition, the samples underwent a surface treatment resulting in surfaces either with or without an interfacial layer. Within the context of this manuscript, films lacking an interfacial layer will be denoted as sample A, while those with an interfacial layer will be referred to as sample B. This layer was then treated presuming that the bulk of the film is electrically in series with the interfacial layer.

3. Materials Characterization

The film microstructure and crystal structure were characterized. X-ray Diffraction (XRD, X'Pert Pro MPD diffractometer, PANalytical, Almelo, The Netherlands) was employed to investigate the structural properties and orientation of the films, using Cu Kα radiation at an accelerating voltage of 40 kV, with each step measured at 0.02° using a 10 second acquisition time for each angle. Diffraction patterns were obtained over a 2θ range of 20° to 60°. The film's surface morphology was examined using a Leo 1530 field emission scanning electron microscope (FESEM, LEO Electron Microscopy Ltd., Cambridge, England), operating at 5 kV.

Prior to dielectric characterization, films were heated to 500°C for 30 minutes to de-age them. Dielectric measurements were performed using a Lakeshore Cryotronics 8400 series

temperature-controlled probe station in the temperature range of 10–300 K. Films were adhered to the stage of the probe station using GE Varnish to maintain high thermal conductivity. Polarization – electric field (P-E) hysteresis loops and first-order reversal curves (FORC) were measured using custom electronics with a 10x external amplifier (AVC instrumentation 790 Series Power Amplifier) to reach the desired output voltage. FORC were measured from -4E_c to 4E_c, where E_c is the coercive field. The dependence of capacitance as a function of AC field and frequency was measured using a Hewlett Packard 4284A precision LCR meter. The harmonics were measured at 1 kHz using an SR 830 lock-in amplifier (Stanford Research Systems, Sunnyvale, CA).

4. Results and discussion

The cross section of the samples is shown in

Figure 1 (a). 1.7 µm KNN films were grown on a platinized Si substrate, which consists of a (100)-oriented silicon wafer coated with a 200 nm SiO_2 and 25 nm of ZnO, followed by a 200 nm thick bottom platinum electrode. The 1 mm diameter circular Pt/RuO_2 top electrodes were patterned on the KNN films using lithography. The films were prepared with two distinct surface terminations: alkali-rich (sample A, (Na+K)/Nb ratio of 2.6) and alkali-depleted with an interfacial layer (sample B, (Na+K)/Nb ratio of 0.8). Both films are smooth and have a columnar structure (Figure 1c-d). The phase composition of the films determined via x-ray diffraction (XRD) showed a partially (001)-oriented single perovskite

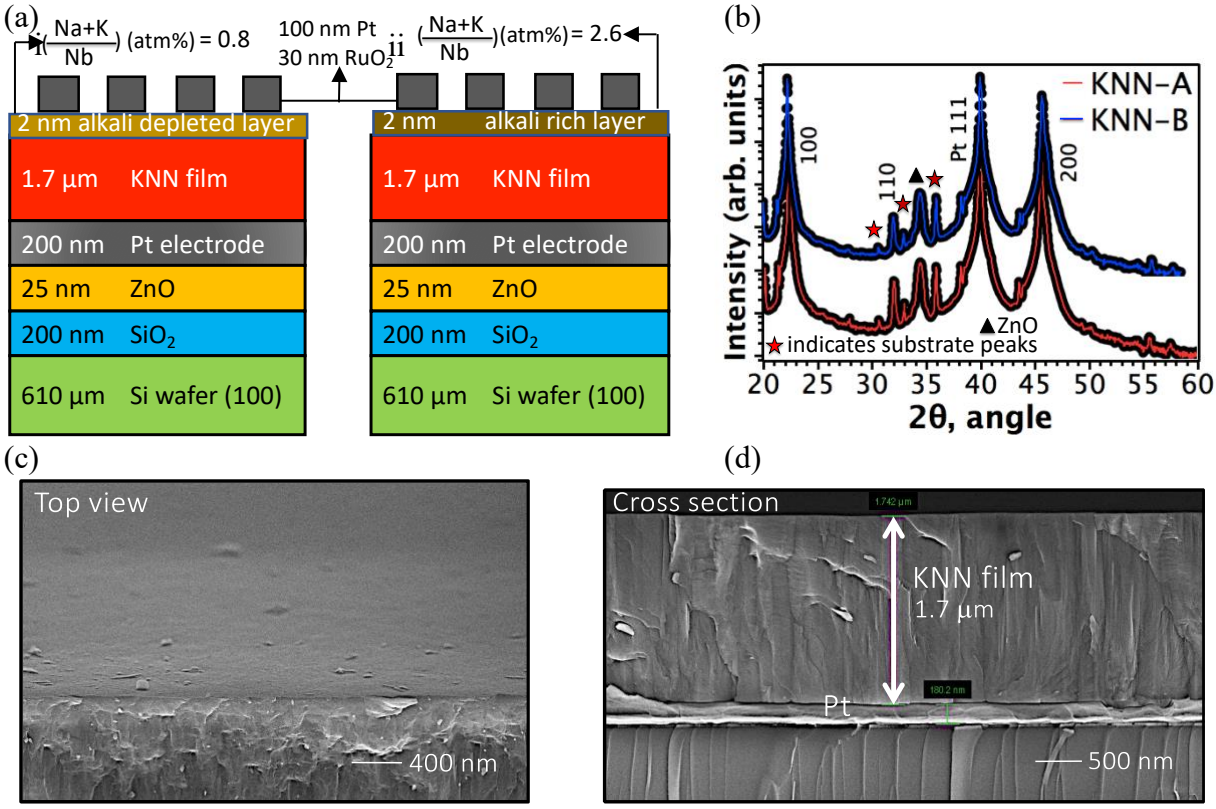

Figure 1: (a) Schematic cross-section of the KNN film stack. Two distinct surface terminations are illustrated: (i) alkali-depleted with a (Na+K)/Nb ratio of 0.8, and (ii) alkali-rich with a (Na+K)/Nb ratio of 2.6, (b) XRD patterns of the films, (c) surface, (d) cross-section FESEM images of the KNN film.

phase (Figure 1b). The key difference between Samples A and B is the presence of an amorphous Si-rich interfacial layer (~2–3 nm thick) at the top interface between the film and the electrode in Sample B. This interfacial layer, associated with alkali-depleted surface termination in KNN films, was confirmed by TEM and SIMS depth profile analyses.[43] Its formation is speculated to result from residual photoresist and/or alkali ion leaching during the photolithography process. The presence of this layer led to a reduction in relative permittivity from 625 ± 5 in Sample A to 481 ± 4 in Sample B, as measured at 1 kHz and 30 mV, along with a decrease in dielectric loss from 0.04 ± 0.01 to 0.03 ± 0.01.

The temperature dependence of the P-E hysteresis loops depicted in **Figure 2** shows that the coercive fields of both samples increase with decreasing temperature, as expected. For measurements conducted at a constant field range of ±400 kV/cm, the remanent polarization of both samples initially decreases upon cooling until approximately 150 K, after which it slightly increases at lower temperatures. The maximum polarization increases with temperature in both samples from 22.9 $\mu C/cm^2$ at 10 K to 30.3 $\mu C/cm^2$ at 300 K for sample A and from 20.7 $\mu C/cm^2$ at 10 K to 31.5 $\mu C/cm^2$ at 300 K for sample B, which is higher than most other reports in the literature, including single crystal data (17 $\mu C/cm^2$ at room temperature) published by Uršič et al.[7]

The minimum in the remanent polarization is attributed to the first-order transition from the low-temperature rhombohedral phase to the orthorhombic phase. Literature data for the rhombohedral-orthorhombic phase transition are summarized in **Table 1**.[27-30] Gomes et al.[31] suggested the presence of an intermediate phase between low temperature rhombohedral and high temperature orthorhombic phases. Recently, second harmonic generation imaging revealed that in $K_{0.5}Na_{0.5}NbO_3$, the rhombohedral and orthorhombic phases coexist between 80 and 190 K, with the rhombohedral phase fraction sharply decreasing between 180 and 200 K, and disappearing above 200 K.[32] Therefore, it is likely that below 250–260 K, gradual phase transitions occur, explaining the observed remanent polarization trends in the KNN films.

Table 1: Summary of literature data on rhombohedral-orthorhombic phase transition in KNN-based systems.

Reference	System	r-o phase transition	Measurement method
Jaffe et al. [27]	$K_{0.5}Na_{0.5}NbO_3$	125 K (-148 °C)	N/A
Baker et al. [28]	$K_{0.5}Na_{0.5}NbO_3$	37 K (-236 °C)	XRD

Attia et al. [30]	$K_{0.5}Na_{0.5}NbO_3$	r phase occurs at 250-260 K as nanoclusters, and at 140 K can be detected by XRD	XRD, simulations (first-principles-derived approach), dielectric measurements
Tellier et al. [29]	$(K_{0.6}Na_{0.4}NbO_3)$ $(K_{0.58}Na_{0.42}NbO_3)$	100–160 K (coexisting with o phase) 100–110 K (coexisting with o phase)	XRD
Orayech et al. [33]	$K_{0.5}Na_{0.5}NbO_3$	135 K	Neutron diffraction
Gomes et al. [31]	$K_{0.5}Na_{0.5}NbO_3$	r below 160 K, 160–265 K intermediate phase, above 265 K orthorhombic phase	Anomalies in the temperature dependence of complex relative permittivity
Li et al. [32]	$K_{0.5}Na_{0.5}NbO_3$	80-200 K (coexisting with o phase)	Second harmonic generation spectral imaging of domain structures

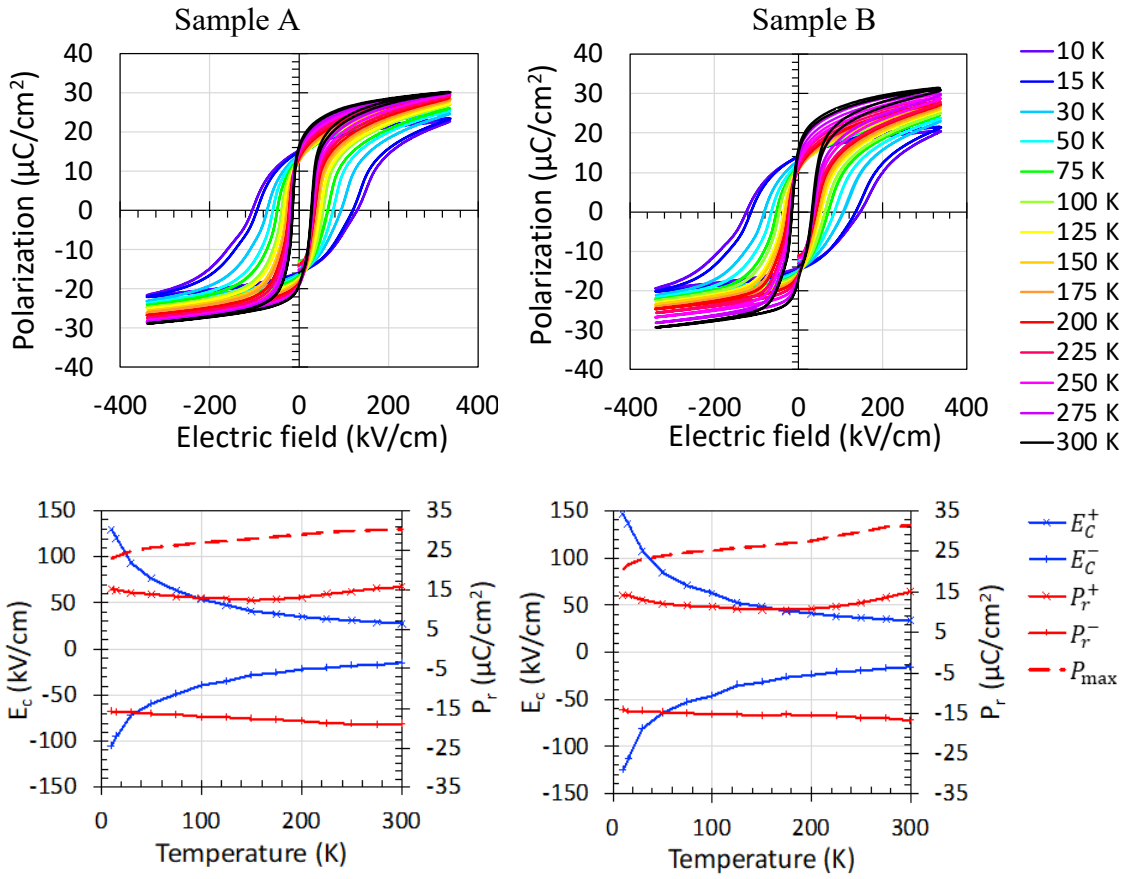

Figure 2: Hysteresis loops and temperature dependence of coercive fields and remanent and maximum polarizations of sample A (left) and sample B (right) from 10 to 300 K.

Figure 3 compares the polarization-electric field (P-E) hysteresis loops at 10 K for the two films. Higher coercive fields were observed in Sample B. The presence of a non-ferroelectric interfacial layer in Sample B can hinder the domain switching process, necessitating a higher electric field to achieve polarization reversal. This increases the energy barrier for domain nucleation and growth, thereby resulting in larger coercive fields.

Additionally, this interfacial layer can alter the overall electric field distribution within the ferroelectric film, further contributing to the observed increase in coercive fields.

In sample B, the P-E loops indicate a leaky interface, as evidenced by the rounded tip of the hysteresis loop at positive fields. In contrast, the tips of the loop are significantly sharper for sample A under the same electric field conditions. This suggests that the higher leakage observed for positive fields in sample B is due to the increased defect concentration associated with the interfacial layer near the top Pt electrode. Secondary Ion Mass Spectrometry (SIMS) depth profiling, combined with Thermally Stimulated Depolarization Current (TSDC) measurements from our ongoing study, indicates that this interfacial region is strongly alkali-depleted, leading to the formation of both alkali and oxygen vacancies.[43] The TSDC measurements revealed two distinct features associated with the depolarization of space charge, likely caused by the migration of mobile ionic species. The corresponding activation energies were found to be approximately 0.7 eV and 1.1 eV. The first peak is consistent with activation energies reported for oxygen vacancy migration in perovskite systems such as PZT, $BaTiO_3$, and $SrTiO_3$.[49–51] The second, higher-energy peak was more pronounced under greater alkali depletion, suggesting its origin lies in the migration of alkali vacancies."

Moreover, the presence of a non-ferroelectric layer at the surface of a ferroelectric film also reduces the net remanent polarization observed in the ferroelectric film. This was attributed to several potential factors: (1) a decrease in the active volume of the ferroelectric material, (2) impeded domain wall movement due to increased defect density, and (3) alteration of the local electric field distribution. To further investigate the decrease in electrical properties due to the presence of an interfacial layer, Rayleigh and Preisach analyses were conducted on both samples at 10-300K.

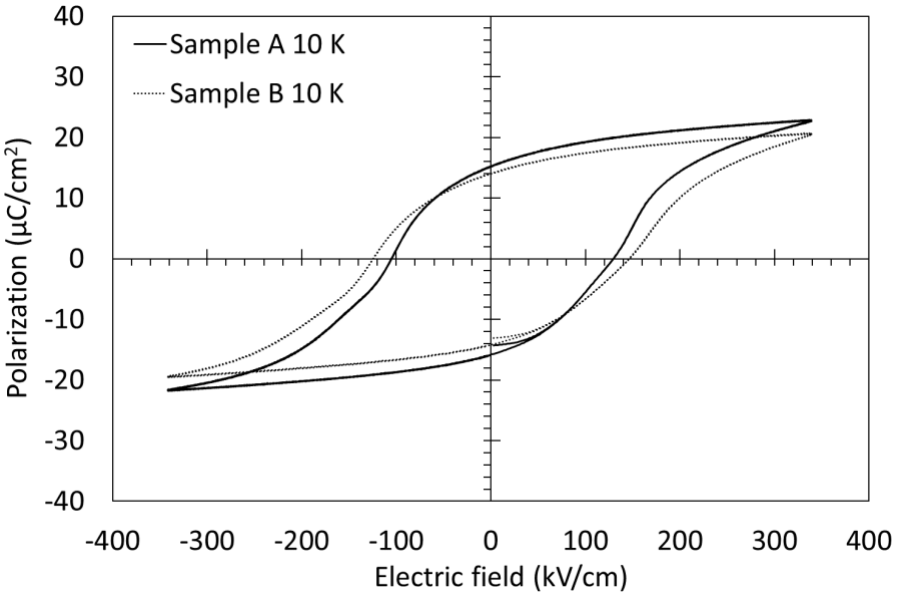

Figure 3: Comparison of Polarization-Electric Field hysteresis loops of sample A and B at 10 K.

To explore if the presence of the interfacial layer alters the relative permittivity of the KNN film, the relative permittivity of the interfacial layer ($\varepsilon_{r,interfacial}$) was estimated under the assumption that the bulk relative permittivity of Sample B is equivalent to the relative permittivity of Sample B), as illustrated in Figure 4. The $\varepsilon_{r,interfacial}$ was then estimated using equation 1:

where C_B is the KNN film with alkali depleted termination (Sample B), C_i is interfacial capacitance, C_A is the capacitance of the KNN film with alkali rich surface termination.

$$\frac{1}{C_B} = \frac{1}{C_A} + \frac{1}{C_i} \qquad \text{Equation 1}$$

At low temperatures (10-30K), where domain wall mobility should be significantly reduced, the estimated relative permittivity of the

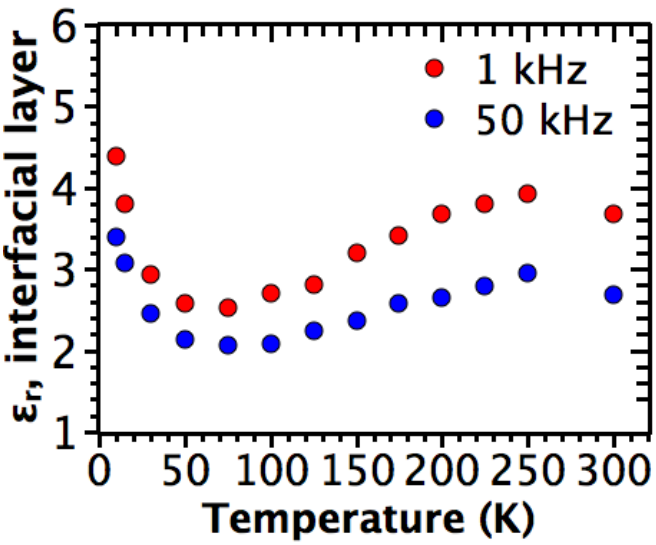

Figure 4: Temperature dependence of the estimated. $\varepsilon_{r,\text{interfacial}}$ was estimated at 1 kHz and 50 kHz under the assumption that the small signal relative permittivity of Sample A and the bulk small signal relative permittivity of Sample B are equivalent.

interfacial layer is around 4-4.4, which is close to the relative permittivity of silica glass. As temperature increases, the interfacial relative permittivity, estimated from the total low-field relative permittivity of the films, remains relatively stable, exhibiting values between 2.5 and 4. The observed variations may be attributed to differences in domain configurations or domain wall mobilities between the two films, particularly as the bulk material undergoes a phase transition. Thus, at least part of the reduction in relative permittivity and high field polarization of Sample B is due to a decrease in the effective electric field within the bulk of the KNN film.

To mitigate the effect of the interfacial layer on the Rayleigh analysis in sample B, a series capacitor model was applied to analyze the relative permittivity data using Equation 1. In the rest of the paper, the interfacial relative permittivity was assigned a relative permittivity of four, and was treated as field and temperature-independent, which is reasonable for such a low relative permittivity layer.

Rayleigh analysis was performed as a function of temperature from 10 K up to 300 K for both Samples A and B. The Rayleigh coefficients, ε_{init} and α were determined from the intercept and slope of the relative permittivity data vs electric field, respectively. The ε_{init} represents the sum of the intrinsic contribution and reversible domain wall motion, while α describes the irreversible domain wall motion contribution to the properties (Equation 2).[44-45]

$$\varepsilon_r = \varepsilon_{init} + \alpha E_{AC} \qquad \text{Equation 2}$$

Figure 5 shows the variation in ε_{init} over a temperature range of 10 to 300 K for Samples A and B with and without an interfacial layer. The ε_{init} of Sample B increases after applying the capacitor in series model, becoming comparable to that of Sample A at 10-50 K,

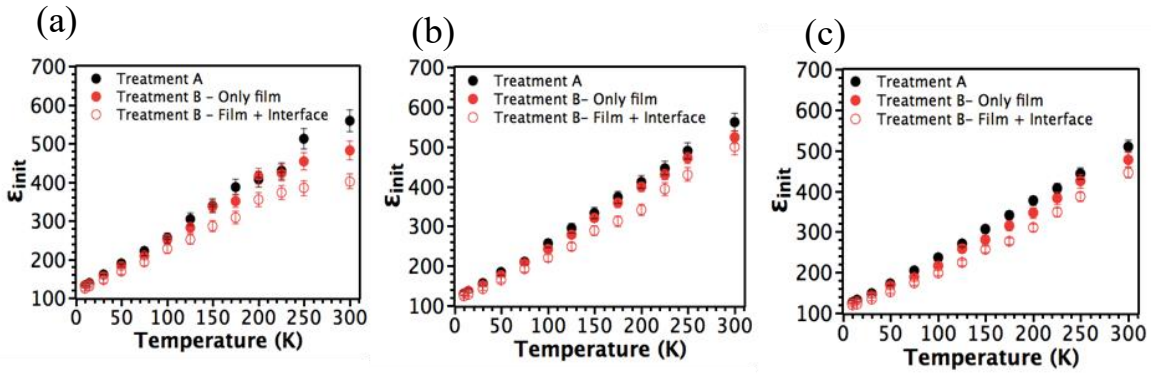

Figure 5 Temperature dependence of the Rayleigh parameter ε_{init} in Samples A and B before (film + interface) and after (only film) applying the capacitor in series model, at (a) 100 Hz, (b) 1 kHz, and (c) 50 kHz.

temperatures at which domain wall motion is frozen out.[46] This is reasonable; since both samples are processed in the same way, the intrinsic contribution to ε_{init} is expected to be the same. Moreover, there should be no dielectric anisotropy when the samples are fully embedded in the rhombohedral phase field.

As temperature increases, the ε_{init} of Sample B increases by up to 11% due to the correction for the capacitor in series, but it remains lower than that of Sample A. This difference becomes more pronounced with rising temperature. In principle, the deviation in ε_{init} may result from differences in either the intrinsic contribution and/or reversible domain wall motion. Here, the differences are tentatively ascribed to subtle differences in the phase transition from the rhombohedral to the orthorhombic phase. The continuous increase in P_r with increasing temperature suggests that the phase transition may not be complete up to 300 K. Thus, at higher temperatures (150-300K), a coexistence of rhombohedral and orthorhombic phases may be present. If this is the case, then the intrinsic contribution to ε_{init} should be *higher* in Sample B, owing to a larger in-plane component of the polarization vector in the rhombohedral phase and dielectric anisotropy. Therefore, the *lower* ε_{init} values in Sample B are likely to be associated with a lower contribution to the relative permittivity from reversible domain wall motion.

The frequency dependence of the Rayleigh parameters was described presuming a linear change with the log of frequency (f), as has been done elsewhere.[47]

$$\varepsilon_{init} = \varepsilon_{init,i} - B_{\varepsilon init} \log(f)$$
$$\alpha_{\varepsilon} = \alpha_{\varepsilon,i} - B_{\alpha_{\varepsilon}} \log(f)$$

Figure 6 shows the frequency dependence of ε_{init}. The interfacial layer both lowers the extracted value of ε_{init} and slightly reduces its frequency dependence. Nonetheless, ε_{init} is lower for sample B compared to sample A even after applying the capacitor in series model. The intrinsic contribution to ε_{init} should be frequency independent over the measured range.

(a)

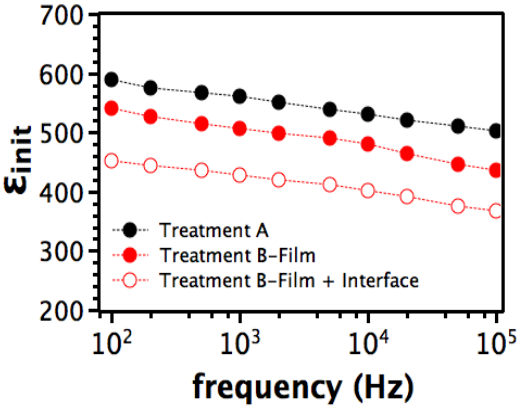

(b)

$B_{\varepsilon initial}$	50 K	100 K	200 K	300 K
Treatment A	4.5±0.2	10.8±0.2	19.7±0.6	28.5±0.7
Treatment B- Film	4.8±0.1	12.1±0.9	22± 1.5	33±2
Treatment B- Film + Interface	4.6±0.2	11.0.±0.6	20± 1.2	28±1

Figure 6 (a) Frequency dispersion of the Rayleigh parameter ε_{init} in Sample A, Sample B before and after applying capacitor in series model at 300K, (b) frequency dependence of ε_{init} at 50, 100, 200, and 300K.

Thus, the reversible contribution to the relative permittivity of sample B appears to be lower than that of sample A.

Figure 7 shows the temperature dependence of the irreversible Rayleigh coefficient α for Samples A and B, before and after accounting for the influence of the interfacial layer. It is clear that the influence of the field drop across the interfacial layer suppresses α.

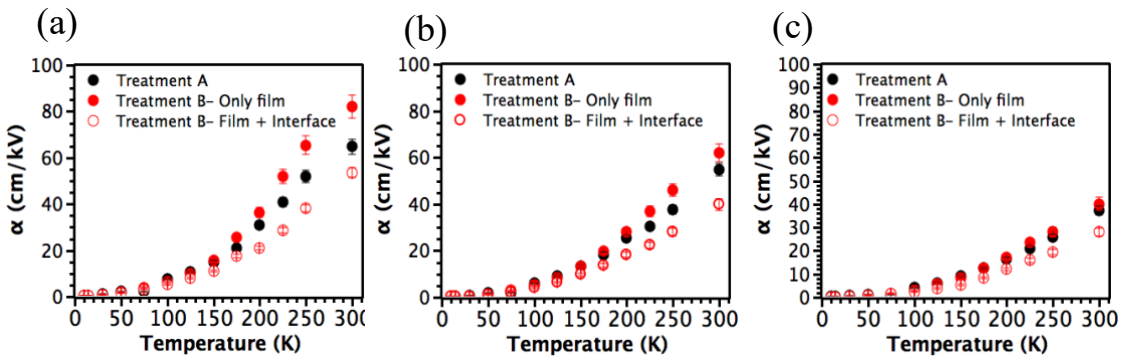

Figure 7 Temperature dependence of the Rayleigh parameter α in Sample A and B before and after applying capacitor in series model, at (a) 100 Hz, (b) 1 kHz, and (c) 50 kHz.

Additionally, α is larger at lower frequencies, as reflected by an increase in $B_{\alpha\varepsilon}$, upon removing the influence of interfacial layer (Figure 8). Assuming that the interfacial layer does not significantly alter the volume fraction of domains, the lower ε_{init} and higher α in Sample B relative to Sample A suggest a shift of some domain walls from reversible to irreversible motion, presumably because of shallow pinning centers associated with the interfacial layer. It was previously demonstrated that a higher concentration of defects, such as $V'_{K,Na}$ or $V_O^{\cdot\cdot}$, associated with the alkali-depleted interfacial layer in Sample B, generates internal fields that can pin domain walls.[37]

(a)

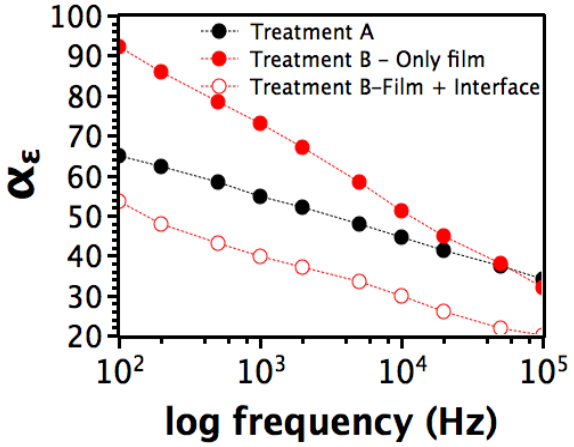

(b)

$B_{\alpha\varepsilon}$	100 K	200 K	300 K
Treatment A	1.3±0.1	5.2±0.1	10.4±0.1
Treatment B- Film	1.2±0.1	7± 0.1	20.3±0.5
Treatment B- Film + Interface	0.9±0.1	4.2± 0.1	10.9±0.3

Figure 8 Frequency dispersion of the irreversible Rayleigh parameter at 300K (b) frequency dependence of α at 50, 100, 200, and 300K.

The $\alpha/\varepsilon_{initial}$ ratio for the two samples is shown in Figure 9. As expected based on the previous discussion, the $\alpha/\varepsilon_{initial}$ ratio increased in Sample B compared to Sample A between 150 and 300K after removing the influence of the interfacial layer.

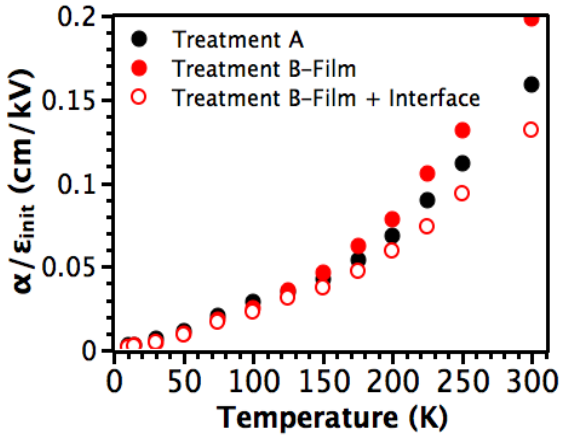

Figure 9 Temperature dependence of $\alpha/\varepsilon_{init}$ ratio for Sample A, Sample B before and after applying capacitor in series model.

The pseudo-activation energies for irreversible domain wall motion were estimated from the Arrhenius plot of log (α) versus 1/T (Figure 10). After accounting for the influence of the interfacial layer, Sample B exhibits a higher pseudo-activation energy compared to Sample A, consistent with a larger coercive field (E_c). As the temperature decreases, the pseudo-activation energies for Sample A and Sample B converge. This suggests that irreversible domain wall motion from deeper wells in Sample B may become frozen out due to the lack of sufficient thermal energy. As a result, only the shallower wells are sampled, causing the pseudo-activation energies to drop with decreasing temperature. At

(a) (b)

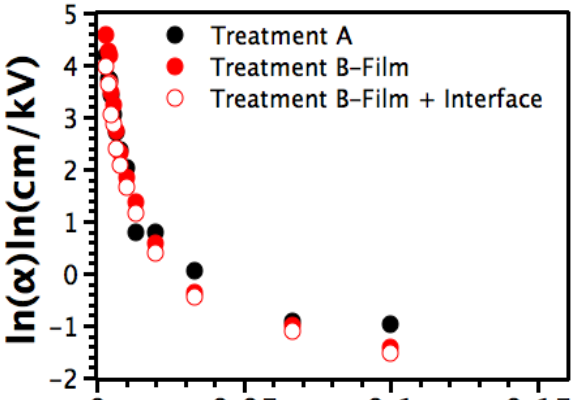

E_a (meV)	150-300 K	10-100 K
Treatment A	37±2 meV	15±1.5 meV
Treatment B- Film	50±3 meV	16±1 meV
Treatment B- Film + Interface	42±2 meV	16±1. meV

Figure 10 Arrhenius plot of the natural log of α vs 1/T to determine the ranges of activation energies for irreversible domain wall motion for Samples A and B before and after applying the capacitor in series model.

10 K, irreversible domain wall motion freezes out and converges to 0; α is 0.23 ± 0.01 cm/kV for Sample A and 0.27 ± 0.02 cm/kV for sample B.

Rayleigh analysis comes with several limitations, such as the need to stay below switching conditions or the assumption that the potential energy barriers have a Gaussian distribution. The Preisach approach, on the other hand, allows investigation of the hysteresis behavior over larger field spans and can be used to treat any distribution of potential energy barriers. The Preisach model is based on the assumption that the P-E loops result from the collective behavior of a set of hysterons, which are rectangular P-E loops with different up (α) and down (β) switching fields.[42]

First-order reversal curves (FORC) were utilized to quantify the Preisach distributions in the KNN films. In **Figure 11**, the reversible Preisach distributions, P_{rev} (i.e., hysteron distributions corresponding to $\alpha = \beta$) for samples A and B are presented. For both samples, P_{rev} is fairly symmetrical around 0 kV/cm and the magnitudes increase with increasing temperature. The P_{rev} peaks of sample B are slightly wider and their magnitude is smaller in comparison to sample A, which is in agreement with Rayleigh analysis results showing lower reversible response in sample B.

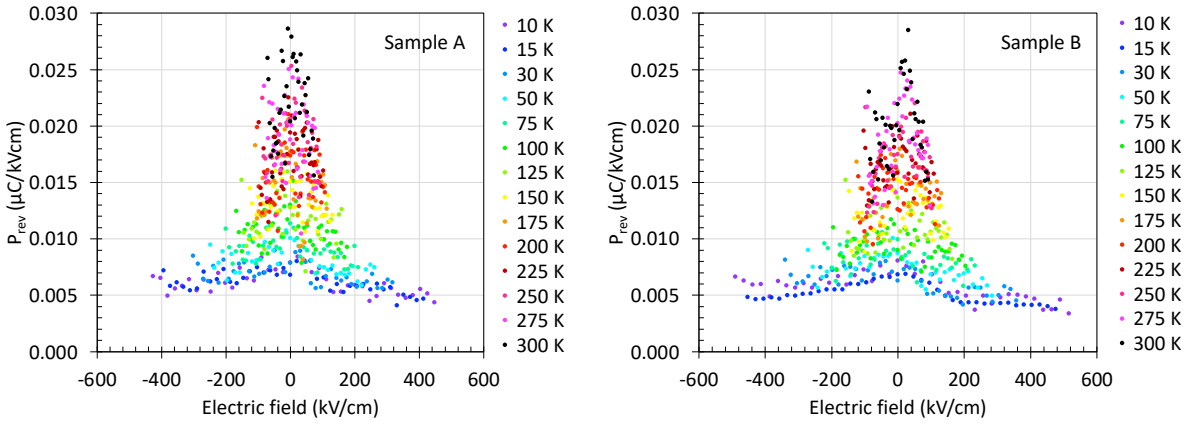

Figure 11: Reversible Preisach distributions of sample A (left) and sample B (right).

The irreversible Preisach distributions (P_{irr}), where $\alpha \neq \beta$, are displayed in Figures 12 and 13. Both samples exhibit a clearly visible peak, with the peak being sharper in Sample A compared to Sample B. This observation aligns with the results of the Rayleigh analysis,

which suggest that differences in barrier height distribution between the two samples may be due to a reduction in the effective electric field in the bulk of Sample B and/or a higher number of pinning sites for domain wall motion caused by the interfacial layer. Additionally, the up- and down-switching fields for the hysterons shift further from the $\alpha = -\beta$ line. This shift is more pronounced in Sample B than in Sample A, suggesting a higher magnitude of imprint in Sample B, consistent with imprint values extracted from P-E hysteresis results. As the temperature increases, the intensity and breadth of the peaks increase, indicating larger polarizations, and a greater variability in the up and down switching fields for the hysterons, respectively. The position of the maxima does not shift with temperature.

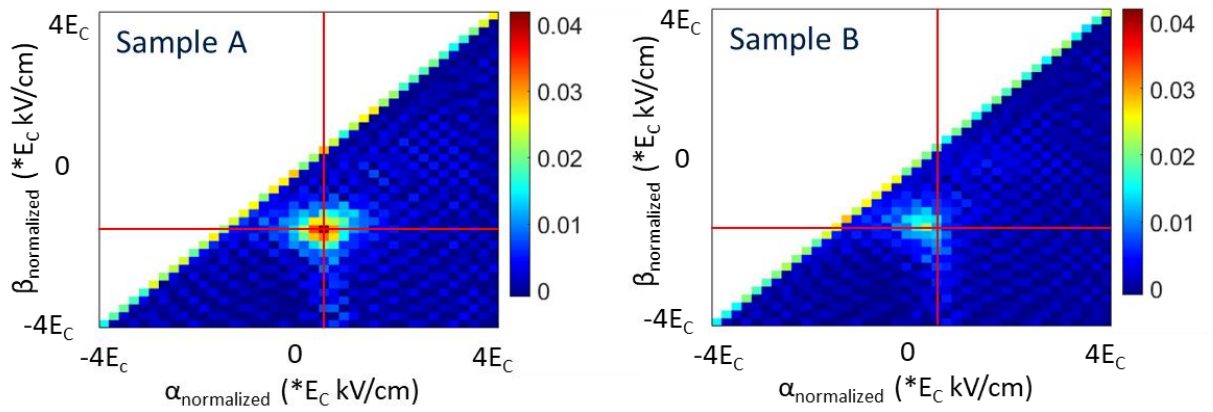

Figure 12: Irreversible FORC distribution at 300 K, sample A (left), sample B (right).

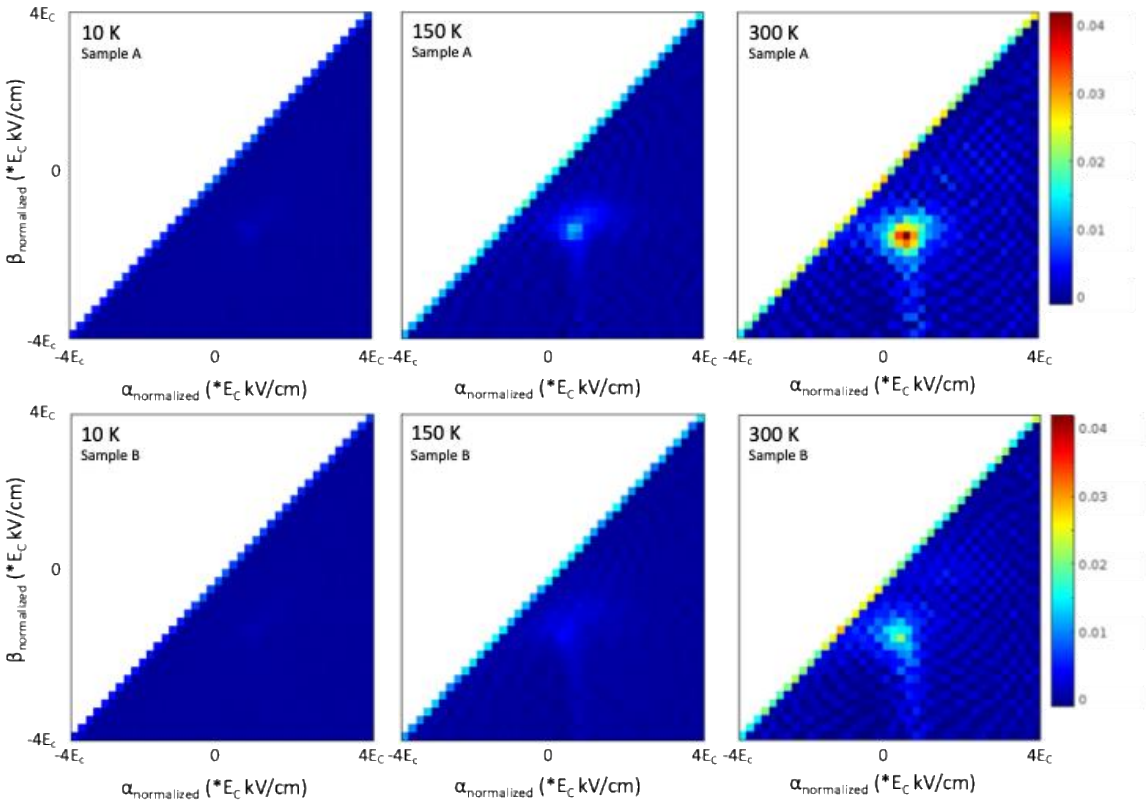

Figure 13: Irreversible FORC distributions at 10, 150 and 300 K.

5. Conclusions

This study examined the effects of surface termination on the dielectric and ferroelectric properties of sputtered KNN thin films. The P-E hysteresis loops revealed that KNN films with an alkali-depleted surface termination attributed to a Si rich amorphous interfacial layer near the top electrode. This layer reduces the effective electric field across the bulk

of the film, resulting in broader P-E loops. Regardless of surface termination, KNN films exhibit an anomalous temperature dependence of remanent polarization, decreasing upon cooling until ~150 K, then slightly increasing due to a rhombohedral-to-orthorhombic phase transition.

The estimated relative permittivity of the interfacial layer at low temperatures (10–30 K) is ~4–4.4, comparable to that of silica glass. It is believed that reduced relative permittivity primarily of samples with alkali-depleted surface layers stems more from a decreased effective electric field rather than domain state changes. Rayleigh analysis shows that alkali-depleted interfacial layer significantly affects both ε_{init} and α. After accounting for the interfacial layer's effects, the ε_{init} in the KNN film alone was 11% higher than when measured in series with the interfacial layer. The lower ε_{init} is attributed to reduced reversible domain wall motion, rather than intrinsic changes. The interfacial layer had an even greater impact on α with an increase of 47% when its influence was removed. Additionally, α increased at lower frequencies due to the depinning of slower-moving irreversible domain walls. The alkali-depleted interfacial layer also produces variations in the energy landscape of pinning sites for domain wall motion and domain switching.

Acknowledgements

The authors gratefully acknowledge Kenji Shibata for providing the KNN films. This work was supported by the National Science Foundation through the Center for Dielectrics and Piezoelectrics under Grant Nos. IIP-1841453 and IIP-1841466, and by the Steward S. Flaschen Professorship. S.H. was supported by a Fulbright-Masaryk Fellowship.

References

1. Setter N, Damjanovic D, Eng L, Fox G, Gevorgian S, Hong S, Kingon A, Kohlstedt H, Park NY, Stephenson GB, Stolitchnov I, Tagantsev AK, Taylor DV, Yamada T, Streiffer S. Ferroelectric thin films: Review of materials, properties, and applications. *J. Appl. Phys.* 2006;**100**(5):051606.
2. Seog HJ, Ullah A, Ahn CW, Kim IW., Lee SY, Park J, Lee HJ, Won SS, Kim SH. Recent progress in potassium sodium niobate lead-free thin films. *J. Korean Phys. Soc.* 2018;**72**(12):1467-1483.
3. Zhang SW, Zhou Z, Luo J, Li JF. Potassium-sodium-niobate-based thin films: Lead free for micro-piezoelectrics. *Ann. Phys.-Berlin* 2019;**531**(7):1800525.
4. Saito Y, Takao H, Tani T, Nonoyama T, Takatori K, Homma T, Nagaya T, Nakamura M. Lead-free piezoceramics. *Nature* 2004;**432**(7013):84-87.
5. Haertling GH. Properties of hot-pressed ferroelectric alkali niobate ceramics. *J. Am. Ceram. Soc.* 1967;**50**(6):329-330.
6. Maeder MD, Damjanovic D, Setter N. Lead free piezoelectric materials. *J. Electroceram.* 2004;**13**(1-3):385-392.
7. Uršič H, Benčan A, Škarabot M, Godec M, Kosec M. Dielectric, ferroelectric, piezoelectric, and electrostrictive properties of $K_{0.5}Na_{0.5}NbO_3$ single crystals. *J. Appl. Phys.* 2010;**107**(3):033705.

8. Shibata K, Oka F, Ohishi A, Mishima T, Kanno I. Piezoelectric properties of (K,Na)NbO_3 films deposited by RF magnetron sputtering. *Appl. Phys. Express* 2008;**1**(1):011501.
9. Wang LY, Ren W, Yao K, Goh PC, Shi P, Wu XQ, Yao X. Effect of pyrolysis temperature on $K_{0.5}Na_{0.5}NbO_3$ thick films derived from polyvinylpyrrolidone-modified chemical solution. *J. Am. Ceram. Soc.* 2010;**93**(11):3686-3690.
10. Safari A, Abazari M. Lead-free piezoelectric ceramics and thin films. *IEEE Trans. Ultrason. Ferroelectr. Freq. Control* 2010;**57**(10):2165-2176.
11. Kupec A, Malic B, Tellier J, Tchernychova E, Glinsek S, Kosec M. Lead-free ferroelectric potassium sodium niobate thin films from solution: Composition and structure. *J. Am. Ceram. Soc.* 2012;**95**(2):515-523.
12. Chowdhury A, Bould J, Londesborough MGS, Milne SJ. Fundamental issues in the synthesis of ferroelectric $Na_{0.5}K_{0.5}NbO_3$ thin films by sol-gel processing. *Chem. Mat.* 2010;**22**(13):3862-3874.
13. Ozmen O, Ozsoy-Keskinbora C, Suvaci E. Chemical stability of $KNbO_3$, $NaNbO_3$, and $K_{0.5}Na_{0.5}NbO_3$ in aqueous medium. 2018;**101**(3):1074-1086.
14. Patterson EA, Cann DP. Piezoelectric properties and unipolar fatigue behavior of KNN-based Pb-free piezoceramics. *IEEE Trans. Ultrason. Ferroelectr. Freq. Control* 2011;**58**(9):1835-1841.
15. Waqar M, He Q, Chai JW, Lim PC, Yao K, Wang JH. Diverse defects in alkali niobate thin films: Understanding at atomic scales and their implications on properties. *Small* 2022;19:2205137.
16. Wu WB, Wong KH, Pang GKH, Choy CL. Correlation between domain evolution and asymmetric switching in epitaxial $Pb(Zr_{0.52}Ti_{0.48})O_3$ thin films. *Appl. Phys. Lett.* 2005;**86**(7):072904.
17. Wang J, Xia YF, Chen LQ, Shi SQ. Effect of strain and deadlayer on the polarization switching of ferroelectric thin film. *J. Appl. Phys.* 2011; **110:114111**.
18. Zhou Y, Chan HK, Lam CH, Shin FG. Mechanisms of imprint effect on ferroelectric thin films. *J. Appl. Phys.* 2005;**98**(2):9.
19. Chen Y, McIntyre PC. Lead zirconate titanate ferroelectric thin film capacitors: Effects of surface treatments on ferroelectric properties. *Appl. Phys. Lett.* 2007;**91**(7):072910-1-3.
20. Kim WH, Son JY, Shin YH, Jang HM. Imprint control of nonvolatile shape memory with asymmetric ferroelectric multilayers. *Chem. Mat.* 2014;**26**(24):6911-6914.
21. Grossmann M, Lohse O, Bolten D, Boettger U, Schneller T, Waser R. The interface screening model as origin of imprint in $PbZr_xTi_{1-x}O_3$ thin films. I. Dopant, illumination, and bias dependence. *J. Appl. Phys.* 2002;**92**(5):2680-2687.
22. Warren WL, Tuttle BA, Dimos D, Pike GE, AlShareef HN, Ramesh R, Evans JT. Imprint in ferroelectric capacitors. *Jpn. J. Appl. Phys. Part 1 - Regul. Pap. Short Notes Rev. Pap.* 1996;**35**(2B):1521-1524.
23. Pike GE, Warren WL, Dimos D, Tuttle BA, Ramesh R, Lee J, Keramidas VG, Evans JT. Voltage offsets in $(Pb,La)(Zr,Ti)O_3$ thin films. *Appl. Phys. Lett.* 1995;**66**(4):484-486.
24. Contreras JR, Kohlstedt H, Poppe U, Waser R, Buchal C. Surface treatment effects on the thickness dependence of the remanent polarization of $PbZr_{0.52}Ti_{0.48}O_3$ capacitors. *Appl. Phys. Lett.* 2003;**83**(1):126-128.

25. Zhu W, Akkopru-Akgun B, Trolier-McKinstry S. Highly accelerated lifetime testing of potassium sodium niobite thin films. *Appl. Phys. Lett.* 2017;111:212903.
26. Shibata K, Suenaga K, Watanabe K, Horikiri F, Nomoto A, Mishima T. Improvement of piezoelectric properties of (K,Na)NbO_3 films deposited by sputtering. *Jpn. J. Appl. Phys.* 2011;**50**(4):041503.
27. Jaffe B, Cook WR, Jaffe H. Piezoelectric Ceramics, Academic Press; 1971. p.185
28. Baker DW, Thomas PA, Zhang N, Glazer AM. A comprehensive study of the phase diagram of $K_xNa_{1-x}NbO_3$. *Appl. Phys. Lett.* 2009;**95**(9):091903.
29. Tellier J, Malic B, Dkhil B, Jenko D, Cilensek J, Kosec M. Crystal structure and phase transitions of sodium potassium niobate perovskites. *Solid State Sci.* 2009;**11**(2):320-324.
30. Attia J, Bellaiche L, Gemeiner P, Dkhil B, Malic B. Study of potassium-sodium-niobate alloys: A combined experimental and theoretical approach. *J. Phys. IV* 2005;**128**:55-60.
31. Gomes MM, Vilarinho R, Pinho R, Almeida A, Noudem JG, Costa MEV, Vilarinho PM, Moreira JA. Revisiting the phase sequence and properties of $K_{0.5}Na_{0.5}NbO_3$ ceramics sintered by different processes. *Ceram. Int.* 2021;**47**(6):8308-8314.
32. Li W, Ma YP, Feng TY, Du ZW, Liu YX, Kalinin SV, Li JF, Li Q. Delineating complex ferroelectric domain structures via second harmonic generation spectral imaging. *J. Materiomics* 2023;**9**(2):395-402.
33. Orayech B, Faik A, Lopez GA, Fabelo O, Igartua JM. Mode-crystallography analysis of the crystal structures and the low- and high-temperature phase transitions in $Na_{0.5}K_{0.5}NbO_3$, *J. Appl. Crystallogr.* 2015;**48**:318-333.
34. Rayleigh L. XXV. Notes on electricity and magnetism—III. On the behaviour of iron and steel under the operation of feeble magnetic forces, 1887;**23**(142):225-245.
35. Néel L. Théorie des lois d'aimantation de Lord Rayleigh: II Multiples domaines et Champ coercitif. 1943;**13**:18-30.
36. Damjanovic D, Demartin M. The Rayleigh law in piezoelectric ceramics. *J. Phys. D-Appl. Phys.* 1996;**29**(7):2057-2060.
37. Damjanovic D. Hysteresis in Piezoelectric and Ferroelectric Materials, in: I. Mayergoyz, G. Bertotti (Eds.), The Science of Hysteresis, Elsevier, 2005.
38. Bassiri Gharb N, Fujii I, Hong E, Trolier-McKinstry S, Taylor DV, Damjanovic D. Domain wall contributions to the properties of piezoelectric thin films. *J. Electroceram.* 2007;**19**(1):49-65.
39. Denis LM. The Infulence of Clamping and Residual Stress on Scaling Effects in $Pb(Zr_{0.3}Ti_{0.7})O_3$ Thin Films for Piezomemes Applications, Ph.D. Thesis. Dissertation, Pennsylvania State University, 2019.
40. Fontanella J, Johnston RL, Sigel GH, Andeen C. Dielectric properties of as-received and gamma irradiated fused silica. *J. Non-Cryst. Solids* 1979;**31**(3):401-414.
41. Damjanovic D. Logarithmic frequency dependence of the piezoelectric effect due to pinning of ferroelectric-ferroelastic domain walls. *Phys. Rev. B* 1997;**55**(2):R649-R652.
42. Fujii I. Dielectric Nonlinearity of Ferroelectrics, Ph.D. Thesis. Dissertation, Pennsylvania State University, 2010.
43. Akkopru-Akgun B., Shibata K., Trolier-McKinstry S., Engineering surface termination for enhanced electrical reliability in KNN thin films. to be submitted to Sci Reports.

44. Damjanovic D, Demartin M. The Rayleigh law in piezoelectric ceramics. J. Phys. D. Appl. Phys. 1999;29:2057–2060.
45. Trolier-McKinstry S, Bassiri Gharb N, Damjanovic D. Piezoelectric nonlinearity due to motion of 180° domain walls in ferroelectric materials at subcoercive fields: A dynamic poling model. Appl. Phys. Lett. 2006;88:202901.
46. Cross LE. Ferroelectric materials for electromechanical transducer applications. Jpn. J. Appl. Phys. 1995;34:2525-2532.
47. Bintachitt P, Jesse S, Damjanovic D, Han Y, Reaney IM, Trolier-McKinstry ., Kalinin SV, Nattermann T. Collective dynamics underpins Rayleigh behavior in disordered polycrystalline ferroelectrics. *Proc. Natl. Acad. Sci.* 2010;107: 7219–7224.
48. Shibata K., Watanabe K., Kuroda T., and Osada T. KNN lead-free films grown by sputtering. Appl. Phys. Lett. 2022;121: 092901-1-5
[49]Wang R-V., McIntyre P.C. [18]O tracer diffusion in $PbZrTiO_3$ thin films: A probe of local oxygen vacancy concentration. *J. Appl. Phys.* 2005;97: 023508-1-8.
[50]Zafar S., Hradsky B., Gentile D., Chu P., Jones R.E., Gillespie S. Resistance degradation in barium strontium titanate thin films. *J. Appl. Phys.* 1999;86, 3890–3894.
[51]Yoon S-H., Randall C.A., Hur K-H. Difference between resistance degradation of fixed valence acceptor (Mg) and variable valence acceptor (Mn)-doped $BaTiO_3$ ceramics. *J. Appl. Phys.* 2010;108: 064101-1-8.